Green, K., & Krauskopf, B. (2009). Dynamics of patterns in lasers with delayed feedback.

Dynamics of patterns in lasers with delayed feedback

Kirk Green, TNO Delft, The Netherlands
Bernd Krauskopf, University of Bristol, UK

June 2009

1 Introduction

Modern semiconductor lasers are small, easy to produce in large numbers and very efficient in terms of turning electrical energy into coherent light. These attractive properties are the reason that semiconductor lasers are today found in their millions in numerous technological applications, including optical communication networks and optical storage systems. On the negative side, semiconductor lasers are very susceptible to external optical influences, especially in the form of delayed feedback due to reflections from external optical elements and/or (bi-directional) coupling to other lasers. The delay arises due to the travel time of the light before it (re)enters the laser. Compared to the very fast time-scales of the dynamics inside a semiconductor laser (on the order of picoseconds), distances between optical components on the order of centimeters already result in considerable delays that cannot be neglected; see, for example, [22, 24] as entry points to the extensive literature.

We are concerned here with the simplest case of a semiconductor laser with conventional optical feedback (COF) in the form of reflections from a standard mirror at some distance from the laser. In fact, even very small amounts of COF, on the order of 0.1% of the output light, may destabilize the laser [11, 29]. This is why in practical applications expensive optical isolators must be employed when a semiconductor laser is coupled to optical fibers or other elements. The now classical case is that of a single-mode edge-emitting laser (EEL) subject to COF. In an EEL — the most commonly used semiconductor lasers today — light is produced in an active region in the shape of a one-dimensional waveguide (with a length of several hundred micrometers up to millimeters); the light exits at one (or both) of the laser's side facets, which act as (semi-transparent) mirrors; see Fig. 1(a). Despite being quite long in the direction of lasing, single longitudinal mode operation of EELs can be ensured, for example, by incorporating internal frequency selective elements into the EEL. What is more, most EELs have a quite narrow active region (of a few micrometers) so that they generally lase at a single transverse mode. This means that the pattern of laser light at the exit facet consists of a single spot under all operating conditions. Because of these properties, an EEL can be described in a rate equation approach by differential equations for the evolution of the (complex-valued) electric field and the density of charge carriers (or inversion) inside the laser. In the presence of

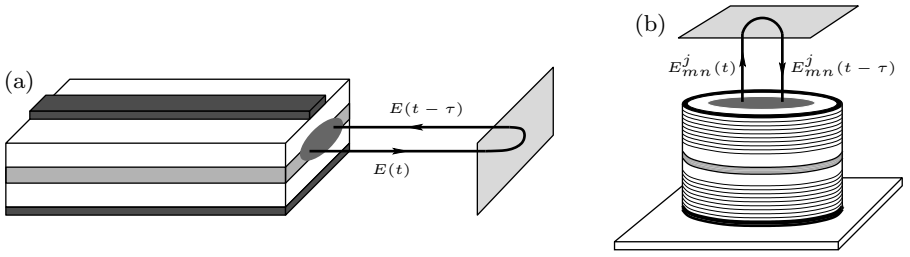

Figure 1: Sketches of an EEL with COF (a), and of a VCSEL with COF (b).

COF the electric field is coupled back to itself after a single fixed delay τ, and this results in the now famous Lang-Kobayashi (LK) equations [28]. This delay differential equation (DDE) has been shown in numerous studies to describe experimental measurements very well (for weak to moderate COF); see, for example, [11, 18, 19].

The question arises what dynamics may ensue in the presence of COF when the laser supports more than one pattern of light at its exit facet. An example of such a laser is a broad-area EEL, where the active region is so wide that the light generally exits the laser not as a single wide spot, but as a one-dimensional pattern of light that consists of a number of bright spots; see, for example, [20, 31]. We do not discuss broad area lasers here, but rather concentrate on the case that the aperture of the laser is truly two dimensional. Namely, we consider vertical-cavity surface-emitting lasers (VCSELs) — an increasingly important type of semiconductor laser with a cylindrical geometry, where a very thin, spatially extended active region is located between two stacks of mirrors. A VCSEL is pumped electrically via a circular contact and its light exits at the top face from a disk-shaped aperture; see Fig. 1(b). VCSELs are even more efficient than EELs and they are more easily integrated (on-chip) into larger arrays or optical circuits. Another advantage is that VCSELs provide consistent single longitudinal mode operation without additional elements (due to the very thin active region). On the other hand, because of the spatial extent of their active region and corresponding aperture, a VCSEL may support several transverse optical modes. In other words, the light does not always exit the VCSEL in a single large spot but generally in a two-dimensional pattern of bright spots on the disk-shaped aperture. The number of transverse optical modes, or patterns of light, that a VCSEL supports increases with the diameter of the aperture [4, 20].

We consider here a VCSEL with COF in the presence of more than one transverse optical mode. As opposed to the case of edge emitting lasers, the modeling of VCSELs is still in development and under some dispute. However, due to the two-dimensional nature of the active region, a VCSEL needs to be described mathematically by partial differential equations for the electric field and the inversion, and we follow here the modelling approach taken in [41]. When subject to COF, the overall model takes the form of a delayed

partial differential equation (DPDE). Note that DPDE models have recently also been considered in other application areas, including the control of spatial patterns [34, 39] and dynamics testing methods for mechanical systems [27]. To analyze or even simulate a DPDE one generally needs to resolve the spatial part of the system with a suitable expansion method (for example, by spatial discretization or Galerkin projection). After truncation this leads to a (possibly quite large) system of DDEs. In [15] we presented an eigenfunction expansion method (EEM) that exploits the physical properties of the VCSEL in order to obtain a DDE that describes the spatio-temporal dynamics of the transverse modes under the influence of COF.

For the case of a VCSEL with COF that supports only two rotationally symmetric transverse optical modes the EEM-reduced DDE is of quite low dimension, yet still describes the dynamics of the system accurately. This makes it possible to perform a bifurcation analysis with advanced numerical continuation tools of constant-intensity solutions, called external cavity modes (ECMs), and even of oscillating-intensity solutions. As a specific example of this new capability we study here how the amount of self-feedback versus cross-feedback of the two spatial modes influences stability regions of ECMs and periodic solutions in the plane of feedback phase and feedback strength of the light as it re-enters the laser. This is of practical interest because it is very difficult experimentally to determine how much the spatial modes influence each other via a COF loop. Our starting point is the observation that, in the degenerate case of pure self-feedback, the ECM structure of the two-mode VCSEL with COF is effectively that of a single-mode laser with COF. We then consider the transition to pure cross-feedback between the two modes. More specifically, we present how the two-parameter bifurcation diagram (in the plane of feedback phase and feedback strength) changes with the amount of self- versus cross-feedback. Each bifurcation diagram consists of codimension-one bifurcation curves that meet and interact at points of higher codimension. Qualitative changes in the bifurcation diagrams are identified in the transition from pure self-feedback to pure cross-feedback. Overall, we find a number of intermediate regimes that differ so much that they might be used for characterizing the nature of the feedback in an experiment.

The chapter is organised as follows. In Sec. 2 we briefly summarize the single mode COF laser as described by the LK equations. The EEM-reduced DDE model of a two-mode VCSEL is introduced in Sec. 3. The bifurcation analysis of its ECMs is the topic of Sec. 4, and the stability of bifurcating periodic solutions is discussed in Sec. 5. The final Sec. 6 summarizes and discusses directions for future research.

2 Single-mode laser with COF

In numerous studies it has been shown that the single-mode COF laser is described well by rate-equations for the complex electric field E and the carrier population N; see, for example, [11, 18, 19]. These rate equations have been introduced by Lang and Kobayashi [28], and they can be written in dimensionless form as

$$\frac{dE}{dt} = (1+i\alpha)EN + \kappa e^{iC_p}E(t-\tau), \tag{1}$$

$$T\frac{dN}{dt} = P - N - (1+2N)\left|E\right|^2. \tag{2}$$

Here P is the pump current, T is the ratio between carrier and photon decay times, and α is the line-width enhancement factor. The last term in Eq. (1) models the optical feedback from the external mirror; here the delay τ is given as the fixed external round-trip time, κ is the (real-valued) feedback strength, and C_p is the feedback phase (describing the sub-wavelength interaction between $E(t)$ and $E(t-\tau)$). The feedback phase C_p is used as one of our bifurcation parameters. In the representation of the results it is helpful that C_p is 2π-periodic, which can be expressed as its invariance under the translation

$$C_p \to C_p + 2\pi. \tag{3}$$

Note that C_p has been shown to be accessible experimentally, allowing for an excellent comparison with numerical solutions of the LK equations (in the short external cavity regime) [18].

Because of the feedback term, system (1)–(2) is a DDE with a single fixed delay and, as such, it has as its phase-space the infinite-dimensional space $C[-\tau,0]$ of continuous functions with values in (E,N)-space. This is due to the fact that an entire history over the interval $[-\tau,0]$ needs to be known to determine the future evolution of Eqs. (1)–(2). In particular, this means that already the basic stability analysis of solutions of DDEs is much more involved than for (the non-delayed case of) ordinary differential equations (ODEs). Namely, equilibria and periodic solutions of Eqs. (1)–(2) have stability spectra consisting of infinitely many eigenvalues [17]. Fortunately, it is possible to perform a numerical bifurcation analysis of a given DDE with the recently developed software tools `DDE-BIFTOOL` [7] and `PDDE-CONT` [37]; see also the survey papers [23, 35].

The basic solutions of Eqs. (1)–(2) are known as CW-states or *external cavity modes* (ECMs), and they are of the form

$$(E,N) = (R_s e^{i\omega_s t}, N_s), \tag{4}$$

where $R_s, \omega_s, N_s \in \mathbb{R}$. The ECMs arise due to the underlying S^1-symmetry of Eqs. (1)–(2) that is given by multiplication of the electric field with a complex number of modulus one, that is, by the transformation $E \mapsto cE$ for any

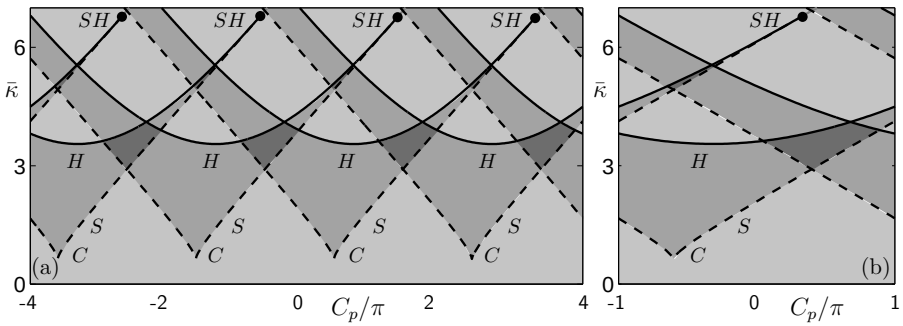

Figure 2: Two-parameter bifurcation diagram of ECMs of the LK equations (1)–(2) in the (C_p, κ)-plane. Panel (a) shows C_p over a wide range to bring out the 2π translational symmetry, while panel (a) shows it over one period in the interval $[-\pi, \pi]$. Shown are curves S of saddle-node bifurcation, curves H of Hopf bifurcation, a codimension-two cusp point C, and a codimension-two saddle-node Hopf point SH; black curves correspond to supercritical and grey curves to subcritical bifurcations. Grey shading of increasing intensity indicates the number of simultaneously stable ECMs, here up to three; $P = 8.0$, $T = 750$, $\alpha = 3.0$, $\tau = 500$, and $\bar{\kappa} = \kappa \times 10^3$.

$c \in \mathbb{C}$ with $|c| = 1$; mathematically, an ECM is a group orbit under this symmetry group [25]. (Since R_s, ω_s and N_s are fixed, ECMs are also referred to as fixed points in some parts of the literature.) To study the ECMs of the COF laser one substitutes the ansatz (4) into the governing equations (1)–(2). Real and imaginary parts are then separated, yielding the ECMs as solutions of the transcendental equation

$$\omega_s = \kappa\sqrt{1+\alpha^2}\,\sin(C_p - \omega_s\tau + \arctan(-\alpha)); \tag{5}$$

see also [13, 32, 36]. Given the ECM frequency ω_s, the corresponding values for the carrier population N_s and amplitude R_s can be computed from

$$N_s = -\kappa\cos(C_p - \omega_s\tau + 2n\pi), \quad R_s^2 = \frac{P - N_s}{1 + 2N_s}. \tag{6}$$

Analytical results about the existence of ECMs (and some results about their stability) can be derived from Eqs. (5)–(6); for example, turning points of this equation correspond to saddle-node bifurcations of ECMs; see [13, 36] for details and [8] as an entry point to asymptotic methods.

In order to continue ECMs in parameters and to determine their stability it is necessary to resolve their S^1-symmetry so that every ECM is an isolated solution (rather than a circle in (E, N)-space). This can be achieved by moving to a rotating frame of reference with fixed frequency b, as given by

$$E \to Ee^{ibt}, \quad b \in \mathbb{R}. \tag{7}$$

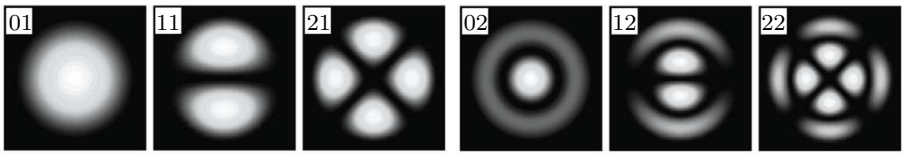

Figure 3: Linearly polarized optical modes LP_{mn} of a VCSEL.

After inserting Eq. (7) into Eq. (1), an ECM can now be studied as a steady state solution for which $b \equiv \omega_s$; see [16, 23] for further details. Figure 2 shows the two-parameter bifurcation diagram of ECMs in the (C_p, κ)-plane, where we fix the laser parameters at $P = 8.0$, $T = 750$ and $\alpha = 3.0$; furthermore, we consider a fixed delay time of $\tau = 500$, which corresponds to a distance of approximately 10 cm between the laser and the mirror. Figure 2(a) shows the bifurcation diagram in the covering space over four periods of C_p, so that the 2π-translational symmetry (3) is clearly visible. The image in Fig. 2(b) shows the bifurcation diagram for $C_p \in [-\pi, \pi]$, that is, over the fundamental domain of (3). The bifurcation diagram has been computed with the package `DDE-BIFTOOL`, and it shows curves S of saddle-node bifurcations and curves H of Hopf bifurcations. These curves divide the (C_p, κ)-plane into regions with different numbers of ECMs. In the light grey region for small κ there is one ECM, which is stable and the continuation of the solitary laser solution (that exists for $\kappa = 0$). Once κ is chosen above the cusp point C, new ECMs may be born in pairs in saddle-node bifurcations, one of which may be initially stable. Stable ECMs lose their stability for increasing κ in Hopf bifurcations, which give rise to stable oscillations of the laser power at the characteristic relaxation-oscillation frequency, on the order of gigahertz. Note that the curves S and H meet at the point SH, which is known as a codimension-two saddle-node Hopf bifurcation [10, 26]. At this point there is a change in the character of the curves S and H from super- to subcritical, meaning that they correspond to bifurcations from which emanate unstable solutions for κ-values above SH. For a more detailed bifurcation analysis of the ECM structure of the COF laser see [13, 36].

3 VCSEL with optical feedback

A VCSEL may support different patterns of light on its aperture. Under the assumption of weak guiding these patterns can be described mathematically as linearly polarized (LP) optical modes, which are roots of the Helmholtz equation [41, 43]. The resulting modes LP_{mn} can be expressed in terms of Bessel functions; they are characterised by n maxima of the Bessel function in the radial direction, and $2m$ zeros in the azimuthal direction of the cylindrical waveguide; some examples of LP modes are shown in Fig. 3.

Following [5, 14, 41, 43], a VCSEL can be described in a rate-equation ap-

proach by PDEs for the evolution of the slowly varying complex electric fields $E^j_{mn}(t)$ of the modes LP_{mn} with polarisation jth, coupled via the real-valued spatial carrier population $N(r,t,\phi)$. (Here the polarisation index j can be either c or s, which denote the two orthogonal cosine and sine instances of the mode LP_{mn}; note that the modes LP_{0n} are rotationally symmetrical, so that they are not distinguished in terms of transverse polarization.) In dimensionless form, one obtains

$$\frac{dE^j_{mn}(t)}{dt} = (1+i\alpha)\xi^j_{mn}(t)E^j_{mn}(t) + F^j_{mn}(t), \tag{8}$$

$$\begin{aligned} T\frac{\partial N(r,\phi,t)}{\partial t} &= \frac{d_f}{r}\left[\frac{\partial}{\partial r}\Big(r\frac{\partial N(r,\phi,t)}{\partial r}\Big)\right] + \frac{d_f}{r^2}\frac{\partial^2 N(r,\phi,t)}{\partial \phi^2} + P(r,\phi,t) \\ &- N(r,\phi,t) - \sum_n \Bigg((1+2\xi_{0n}(t))|E_{0n}(t)|^2 |\Psi_{0n}(r,\phi)|^2 \\ &+ \sum_m \sum_{j=c,s} 2(1+2\xi^j_{mn}(t))\left|E^j_{mn}(t)\right|^2 \left|\Psi^j_{mn}(r,\phi)\right|^2 \Bigg). \end{aligned} \tag{9}$$

The spatial pump $P(r,\phi,t) \equiv P(r)$ describes carrier injection over the core region of the VCSEL via a rotationally symmetric contact. The modal gains ξ^j_{mn} are given by integrals describing the spatial overlap between the respective optical field and the inversion; see [15] for full details. The functions $F^j_{mn}(t)$ describe an external perturbation that is applied to the electric fields of the modes LP_{mn}. In the present case, this external perturbation is optical feedback from a mirror at a fixed distance, meaning that Eqs. (8)–(9) take the form of a delayed PDE. To make this system amenable to a full nonlinear bifurcation analysis one needs to resolve the spatial dependence. As is common [41], the azimuthal direction can be resolved through the use of a Fourier series expansion

$$N(r,\phi,t) = \sum_{k=0}^{\infty} \big(N_{ck}(r,t)\cos(k\phi) + N_{sk}(r,t)\sin(k\phi) \big). \tag{10}$$

The radial direction could be resolved via the use of a finite difference discretization scheme [14, 41]. However, this typically results in a large-scale system of differential equations which are difficult to handle both analytically and numerically. Therefore, we choose to perform a second eigenfunction expansion. Namely, we use a kth order Bessel function expansion [15]

$$N_k(r,t) = \sum_{q=1}^{\infty} N_{kq}(t) J_k(\gamma_{k,q} r). \tag{11}$$

After these two expansions, and after suitable orthogonality conditions have been applied [15], one is left with a spatially resolved system describing a multi-transverse-mode VCSEL (with optical feedback). Importantly, the integral functions that describe the spatial overlaps between the inversion density

with the pump current and the electric field, respectively, take the form of constant coupling constants. Hence, they can be evaluated a priori, which leads to a considerable speed-up in numerical computations; see [15] for full details of the general case.

3.1 EEM-reduced model of a two-mode VCSEL with optical feedback

We consider here in detail the case that the VCSEL supports only the first two rotationally symmetric modes LP_{01} and LP_{02}; see Fig. 3. These symmetric modes are desirable in optical communication schemes for their coupling efficiency, and they may be found stably in certain types of VCSELs, notably those with smaller aperture diameter [4]. The two-mode VCSEL has been studied experimentally in [33], and theoretical studies can be found in [14, 15, 40]. From the mathematical point of view, the LP_{01} and LP_{02} modes can be described by their radial profile alone, which allows for a substantial reduction of the dimensionality of the overall rate equations. Namely, one obtains the dimensionless reduced DDE

$$\begin{aligned}
\frac{dE_1(t)}{dt} &= (1+i\alpha)\xi_1 E_1(t) \\
&\quad +\kappa e^{iC_p}\big[\eta E_1(t-\tau)+(1-\eta)E_2(t-\tau)\big], \qquad (12)\\
\frac{dE_2(t)}{dt} &= (1+i\alpha)\xi_2 E_2(t) \\
&\quad +\kappa e^{iC_p}\big[\eta E_2(t-\tau)+(1-\eta)E_1(t-\tau)\big], \qquad (13)\\
T\frac{dN_q(t)}{dt} &= -(\gamma_{0,q}^2 d_f+1)N_q(t)+\rho_q \\
&\quad -\sum_{n=1}^{2}\left((1+2\xi_n)|E_n(t)|^2\beta_n^{0q}\right). \qquad (14)
\end{aligned}$$

We consider here a total of $q = 14$ expansion terms for the spatial variable N, which was found in previous studies [14, 15] to give sufficient accuracy. (Note that, for ease of presentation, we now write the $N_{kq}(t)$ in Eq. (11) as $N_q(t)$.) Hence, the overall system consists of 18 differential equations in total. Here the $\gamma_{0,q}$ are the roots of the qth Bessel function J_k, and the overlap integrals (which only need to be evaluated once) are given by

$$\begin{aligned}
\xi_n &= \sum_{q=1}^{14}\int_0^1\left(|\Psi_n(r)|^2 N_q J_0(\gamma_{0,q}r)\right)r\,dr, \qquad (15)\\
\rho_q &= \frac{2}{[J_1(\gamma_{0,q})]^2}\int_0^1 P(r)J_0(\gamma_{0,q}r)\,r\,dr, \qquad (16)\\
\beta_n^{0q} &= \frac{2}{[J_1(\gamma_{0,q})]^2}\int_0^1 |\Psi_n(r)|^2 J_0(\gamma_{0,q}r)\,r\,dr. \qquad (17)
\end{aligned}$$

Furthermore, the spatial pump $P(r)$ in Eq. (16) is modeled as

$$P(r) = P_{\max}\big(1 + \operatorname{erf}(2\sqrt{75}(-r + 0.3))\big)/2. \tag{18}$$

The optical feedback has been introduced explicitly into Eqs. (12)–(13) for the electric fields of the modes LP_{01} and LP_{02}, respectively. As was the case for the LK equations in Sec. 2, for each of the two fields the feedback has a common delay time τ, a common strength κ and a common (2π-periodic) phase C_p. The feedback terms depend on the homotopy parameter $\eta \in [0, 1]$, which models the amount of self-feedback versus cross-feedback of the two modes. Specifically, for $\eta = 1$ both modes receive only their own feedback, which we refer to as pure self-feedback; in fact, before the study in [14], only pure self-feedback was assumed when modeling VCSELs with feedback. However, one would expect that the modes are no longer orthogonal in the far-field (at the point of reflection), and/or defects in the external mirror's surface may result in coupling between the modes. In short, one would expect a certain amount of cross-feedback, that is, $\eta < 1$; note that the amount of self- versus cross-feedback as modeled by η might be changed experimentally by mirror shaping or the use of frequency selective feedback [38]. The other extreme is that of pure cross-feedback for $\eta = 0$, where LP_{01} receives feedback only from LP_{02}, and vice versa. Hence, by decreasing η from 1 to 0 we are able to study over the entire range the influence of self- versus cross-coupling on the dynamics of Eqs. (12)–(13) as represented by the bifurcation diagram of ECMs in the (C_p, κ)-plane.

3.2 Analytical results for the two-mode ECM structure

The basic solutions of Eqs. (12)–(14) are ECMs, which now are of the form

$$(E_1(t), E_2(t), N_{1,\dots,14}(t)) = (R_1 e^{i\omega_s t}, R_2 e^{i\omega_s t + i\Phi}, N_{1,\dots,14}), \tag{19}$$

where $R_1, R_2, \omega_s, \Phi, N_1, \dots, N_{14} \in \mathbb{R}$. In other words, both modes have constant but generally different amplitudes R_1 and R_2, which both feed from the same constant reservoir of spatially distributed carriers as expressed by the constants $N_1, \dots, N_{14}$ and Eq. (11). Furthermore, both fields have the same frequency ω_s with a constant phase shift Φ between them. We remark that in reality there is a frequency difference between the two modes, but it is extremely small (only about 1 THz), which motivates modelling the frequencies of the two modes as identical.

The ECMs for the two-mode VCSEL as given by (19) again arise from the underlying S^1-symmetry of Eqs. (12)–(14). It is given by multiplication of *both* electric fields with any complex number of modulus one, that is, by the transformations

$$(E_1, E_2) \mapsto (cE_1, cE_2) \quad \text{for } c \in \mathbb{C} \text{ with } |c| = 1. \tag{20}$$

As was the case for the LK equations, an ECM is a group orbit under this symmetry group; when projected onto the $(R_1, R_2, N_{1\dots14})$-space an ECM can be treated as a steady state solution [25].

As before, we substitute the ansatz (19) into Eqs. (12)–(14) This yields two coupled transcendental equations for the frequency ω_s and the phase difference Φ, which can be written as

$$\begin{aligned}\omega_s &= \kappa\eta\sqrt{1+\alpha^2}\sin\big(C_p-\omega_s\tau+\arctan(-\alpha)\big)\\ &\quad+\kappa(1-\eta)\frac{R_2}{R_1}\sqrt{1+\alpha^2}\sin\big(C_p-\omega_s\tau+\arctan(-\alpha)+\Phi\big), \qquad (21)\\ \omega_s &= \kappa\eta\sqrt{1+\alpha^2}\sin\big(C_p-\omega_s\tau+\arctan(-\alpha)\big)\\ &\quad+\kappa(1-\eta)\frac{R_1}{R_2}\sqrt{1+\alpha^2}\sin\big(C_p-\omega_s\tau+\arctan(-\alpha)-\Phi\big). \qquad (22)\end{aligned}$$

Even though these formulae give a way of eliminating R_1 and R_2, unfortunately, it is not possible to derive a general formula for just ω_s or just Φ. (Alternatively, one could eliminate Φ but then R_1 and R_2 remain.) This situation is analogous to the task of finding the compound laser modes of two mutually delay-coupled lasers [9].

However, we can analyse the ECM structure for the two special cases of pure self-feedback where $\eta = 1$, and of pure cross-feedback where $\eta = 0$. Firstly, for $\eta = 1$ the second terms of (21) and (22) are zero, so that both equations reduce exactly to Eq. (5). Hence, the equation for the ECMs for the two-mode VCSEL with pure self-feedback is exactly the equation for the ECMs of the COF laser. Notice, however, that for the two-mode VCSEL model Eq. (5) represents two identical solutions, which constitutes a degenerate (double-covered) situation. Namely, for $\eta = 1$ the constant Φ shift between E_1 and E_2 can take any value, and one can speak of a Φ-indeterminacy.

For $\eta = 0$, on the other hand, the first terms of (21) and (22) are zero, so that the two transcendental equations reduce to

$$\begin{aligned}\omega_s &= \kappa\frac{R_2}{R_1}\sqrt{1+\alpha^2}\sin\big(C_p-\omega_s\tau+\arctan(-\alpha)+\Phi\big), \qquad (23)\\ \omega_s &= \kappa\frac{R_1}{R_2}\sqrt{1+\alpha^2}\sin\big(C_p-\omega_s\tau+\arctan(-\alpha)-\Phi\big). \qquad (24)\end{aligned}$$

By eliminating R_1 and R_2 we obtain

$$\begin{aligned}(\omega_s)^2 = \kappa^2(1+\alpha^2)&\sin\big(C_p-\omega_s\tau+\arctan(-\alpha)+\Phi\big)\\ &\times\sin\big(C_p-\omega_s\tau+\arctan(-\alpha)-\Phi\big). \qquad (25)\end{aligned}$$

We cannot solve this coupled system, but we can conclude that for $\eta = 0$ the ECMs satisfy the additional π-symmetries given by the translations

$$C_p \mapsto C_p+\pi \quad \text{and} \quad \Phi \mapsto \Phi+\pi. \qquad (26)$$

In particular, this implies that the bifurcation diagram in the (C_p, κ)-plane is invariant under translation of C_p by π (and not only under translation by 2π). We remark that Eq. (25) is very similar to that determining the compound

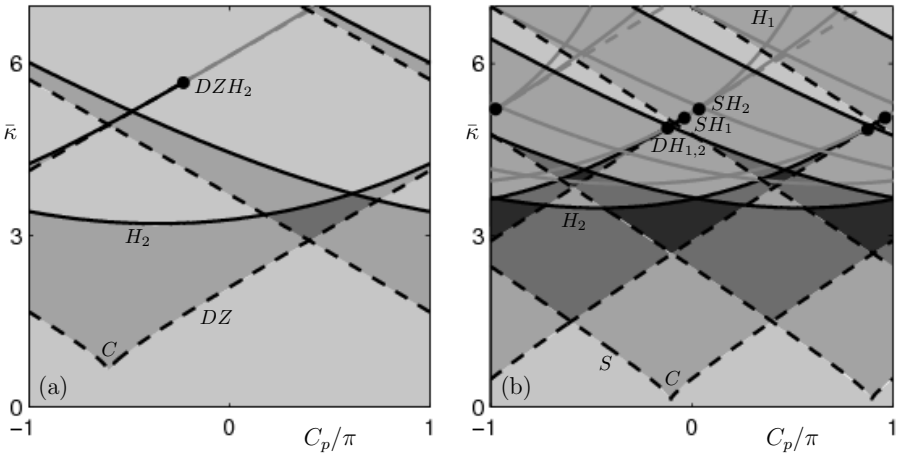

Figure 4: Two-parameter bifurcation diagrams of ECMs of Eqs. (12)–(14) in the (C_p, κ)-plane. Panel (a) shows the double-covered case $\eta = 1.0$, with curves DZ of double-zero eigenvalues and a curve H_2 of Hopf bifurcations. Panel (b) shows the case $\eta = 0.0$, with curves S of saddle-node bifurcation and curves H of Hopf bifurcation. Grey shading of increasing intensity indicates the number of simultaneously stable ECMs; $P_{\max} = 2.0$, $T = 750$, $\alpha = 3.0$, $d_f = 0.05$, $\tau = 500$, and $\bar{\kappa} = \kappa \times 10^3$.

laser modes of two mutually delay-coupled lasers with zero frequency detuning [9]. This suggests that the two-mode VCSEL with pure cross feedback could be interpreted as two spatially extended, mutually delay-coupled VCSELs — one lasing at the LP_{01} mode and the other lasing at the LP_{02} mode, and both having the same free-running frequency. Another requirement is that the two VCSELs would have to have identical carrier dynamics (as they compete for the same carrier reservoir). This latter requirement constitutes the main difference with the case of two mutually delay-coupled *independent* lasers as studied in [9].

Overall, we find that the two extreme cases of pure self-feedback and of pure cross-feedback have different special properties. The main question that we will address next is how the corresponding bifurcation diagrams of ECMs in the (C_p, κ)-plane transform into one another as the homotopy parameter $\eta \in [0, 1]$ is changed.

4 Numerical bifurcation analysis of the two-mode ECM structure

We now perform a numerical bifurcation analysis of the ECMs of Eqs. (12)–(14) with the continuation package `DDE-BIFTOOL` [7]. To this end, we again first resolve their S^1-symmetry (20) by moving to a rotating frame of reference with

frequency b, now given by

$$(E_1, E_2) \to (E_1 e^{ibt}, E_2 e^{ibt}), \tag{27}$$

so that the ECMs can be studied as steady state solutions for which $b \equiv \omega_s$. The ECMs can now be found and continued in parameters. To this end, we fix the material parameters at $P_{\max} = 2.0$, $T = 750$ and $\alpha = 3.0$; furthermore, we set the diffusion constant to $d_f = 0.05$. As before, we consider a fixed delay time of $\tau = 500$, and use the feedback phase C_p and the feedback strength κ as free parameters.

Motivated by the analysis in Sec. 3.2, our starting points are the bifurcation diagrams in the (C_p, κ)-plane of Eqs. (12)–(14) for $\eta = 1.0$ and for $\eta = 0.0$, which are shown in Fig. 4. For the case of pure self-feedback of $\eta = 1.0$ in Fig. 4(a) we find a curve *DZ* of double-zero eigenvalues and a curve H_2 of Hopf bifurcations. The two curves meet at a point, labeled DZH_2, where they change from super- to subcritical, which is indicated by a change of the curves from black to grey. Notice also the cusp point C on the curve *DZ*. The grey shading indicates the number of coexisting stable ECMs in the different regions, of which there are up to three. As was discussed in Sec. 3.2, the bifurcation diagram in Fig. 4(a) is indeed as that for an equivalent COF laser; compare with Fig. 2(b). The difference is that instead of a saddle-node bifurcation (with a single eigenvalue zero) we find a double-zero eigenvalue along the curve *DZ*, which stems from the fact that we are dealing with a degenerate (double-covered) case for $\eta = 1.0$.

The bifurcation diagram for the case of pure cross-feedback for $\eta = 0.0$ is shown in Fig. 4(b). One immediately notices its additional symmetry of translation by π in C_p in accordance with (26). As a result, we find two curves S of saddle-node bifurcations, with two cusp point C in the C_p-interval $[-\pi, \pi]$. Similarly, we find two sets of Hopf bifurcation curves H_1 and H_2, which meet the curves S at codimension-two saddle-node Hopf bifurcations SH_1 and SH_2. In accordance with general results of bifurcation theory, the curves S, H_1 and H_2 change from super- to subcritical at these bifurcation points. The point marked $DH_{1,2}$ is a codimension-two double-Hopf bifurcation, where the curves H_1 and H_2 cross transversally. Grey shading again indicates the number of coexisting stable ECMs in the different regions, of which there are up to four.

4.1 Dependence of the bifurcation diagram on η

We now consider the transition between the two special cases in Fig. 4 as the homotopy parameter η is changed. To give an initial impression, Fig. 5 shows one-parameter bifurcation diagrams for fixed $\kappa = 0.003$ where the power of the first electric field $P_1 = R_1^2$ is plotted against the feedback phase C_p (over the fundamental interval $[-\pi, \pi]$). From panel (a) to (f) η is increased from $\eta = 0.0$ in intermediate steps to $\eta = 1.0$. Hence, Fig. 5(a) and (f) correspond to one-dimensional cross sections at $\kappa = 0.003$ through the two panels of Fig. 4, and the remaining panels illustrate the transition between these two cases. In Fig. 5 parts of the branches are drawn black when the corresponding ECM is stable,

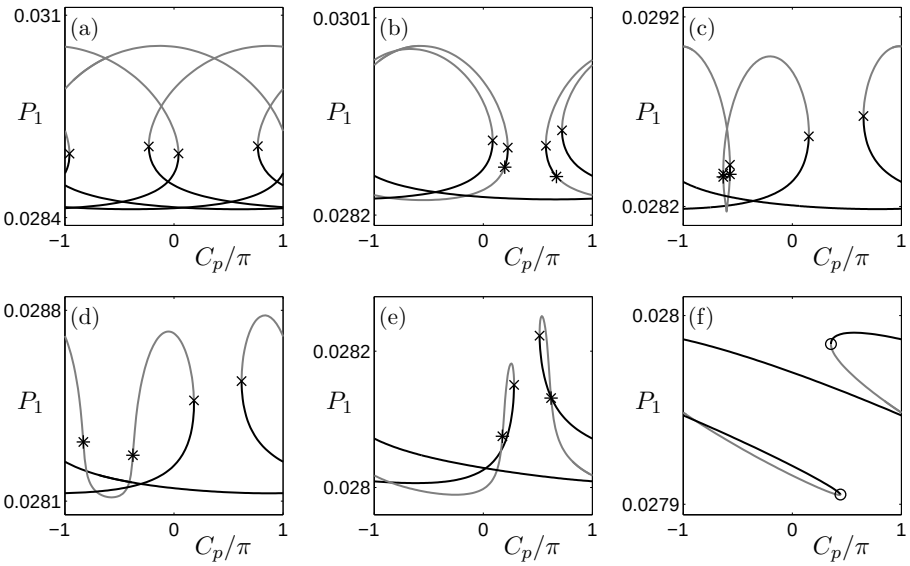

Figure 5: One-parameter bifurcation diagrams showing the power P_1 of LP_{01} against C_p. Stable parts of the branches are black and unstable part grey; marked are saddle-node bifurcations ($\times$), Hopf bifurcations ($*$), and in (f) degenerate double-zero points ($\circ$). From (a) to (f), η takes the values 0.0, 0.3, 0.6, 0.7, 0.9 and 1.0; $\kappa = 0.003$ and the other parameters are as in Fig. 4.

and grey otherwise. Furthermore, saddle-node bifurcations (fold points with respect to C_p) and Hopf bifurcations are marked.

For pure cross-feedback at $\eta = 0$, the ECM branches in Fig. 5(a) exhibit the additional π-symmetry (26). Furthermore, for any value of C_p one finds either three or four stable coexisting ECMs, which agrees with the two-dimensional bifurcation diagram in Fig. 4(b) when crossed at $\kappa = 0.003$. As η is increased from zero the additional π-symmetry is immediately broken. Furthermore, one notices the emergence of Hopf bifurcations, which destabilize parts of the ECM branches. Already in Fig. 5(b) for $\eta = 0.3$ the number of coexisting stable ECMs is reduced to at most two. Notice further that the branches have moved through one another, which leads to a C_p-interval with only one stable ECM. As η is increased further to $\eta = 0.6$ in Fig. 5(c) the Hopf bifurcations move closer to the saddle-node bifurcations near a small loop in the ECM branch. In Fig. 5(d) for $\eta = 0.7$ one finds that this loop has disappeared together with the associated saddle-node bifurcations (that is, fold points). For $\eta = 0.9$ in Fig. 5(e) the two Hopf bifurcation points move towards the remaining two saddle-node bifurcations. Finally, for pure self-feedback at $\eta = 1.0$ in Fig. 5(f) the Hopf bifurcations take place exactly at the fold points. In fact, these points are degenerate double-zero eigenvalue points; compare with Fig. 4(a).

Figure 5 raises some immediate questions. Where do the Hopf bifurcation

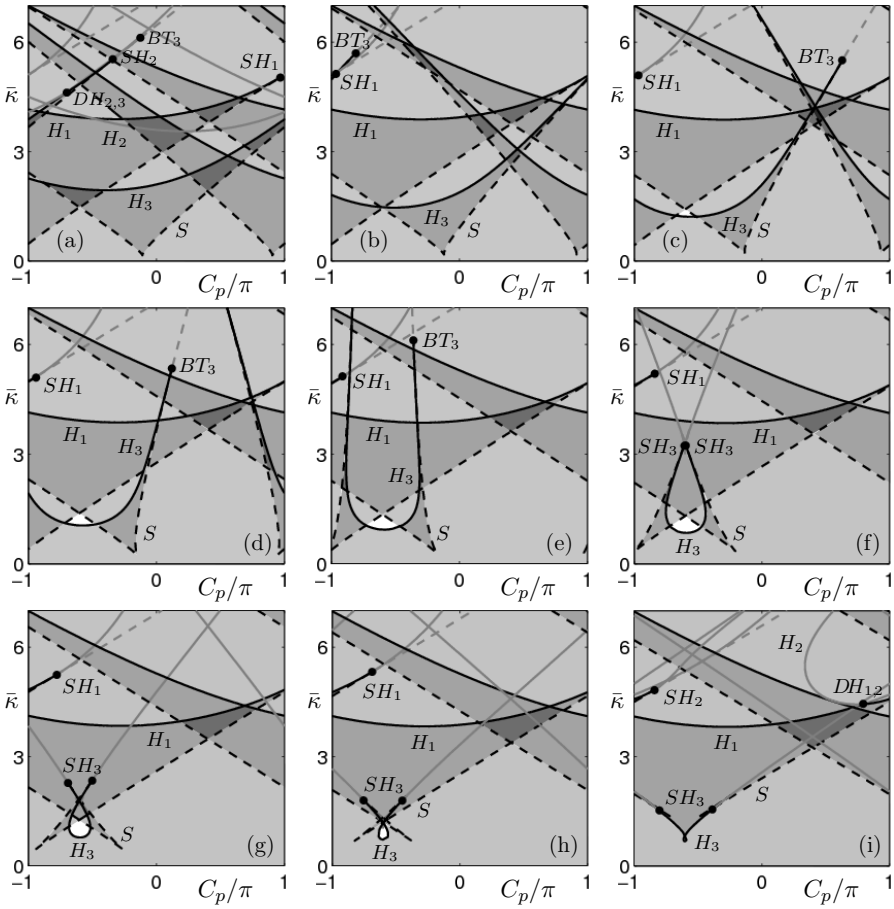

Figure 6: The two-parameter bifurcation diagrams of ECMs of Eqs. (12)–(14) in the (C_p, κ)-plane for increasing values of η. From (a) to (i), η takes the values 0.1, 0.2, 0.3, 0.4, 0.5, 0.6, 0.7, 0.8 and 0.9; other parameters are as in Fig. 4.

points in Fig. 5(b) come from? How do the two saddle-node bifurcation points disappear? Furthermore, what is the mechanism that produces the degenerate double-zero point in the limit $\eta = 1.0$? To answer these questions we now consider the changes of the entire two-parameter bifurcation diagram in the (C_p, κ)-plane with η. Figure 6 shows nine intermediate bifurcation diagrams in η-steps of 0.1, where the bifurcation curves and regions of ECM stability are represented as in Fig. 4. In addition, we now find a white region without stable ECMs, as well as a codimension-two Bogdanov-Takens bifurcation point BT_3 (corresponding to isolated double zero eigenvalues [10, 26]).

Again, a first conclusion from Fig. 6 is that, as η is increased from zero, the additional π-symmetry in C_p is immediately lost; see Fig. 6(a) for $\eta = 0.1$.

In particular, a difference emerges of how the (two sets of) saddle-node and Hopf curves interact. Namely, already for $\eta = 0.3$ as in panel (c) there is a single codimension-two saddle-node Hopf point SH_1 near $C_p = -\pi$, and a single Bogdanov-Takens point BT_3 near $C_p = 0.7\pi$; details of this transition near $\eta = 0.0$ are presented in Sec. 4.2. There is an important distinction between the corresponding Hopf bifurcation curves H_1 and H_3: the ensuing periodic solutions are of two very different types. Namely, when H_1 is crossed well-known relaxation oscillations (ROs) arise. Crossing H_3, on the other hand, results in the emergence of external-cavity oscillations (EOs) with a period of about the external round-trip time τ [15]. Notice further from Fig. 6 that, as η is increased, the Hopf curve H_3 associated with the EOs moves towards lower values of κ. As a result, one would expect to find EOs already for lower values of κ compared to ROs; the stability regions and the bifurcations of ROs and EOs are discussed in more detail in Sec. 5.

As the curve H_3 moves with η, a region without any stable ECMs opens up for $\eta \geq 0.2$. This occurs when H_3 dips below the crossing point of the saddle-node curves; see Fig. 6(b). Increasing η further we find that the Hopf curve H_3 becomes steeper and changes slope; see Fig. 6(e). This is due to the fact that a point of self-intersection of H_3 moves into the chosen κ-range of $[0, 0.007]$, giving rise to a loop of H_3; see Fig. 6(f). The Bogdanov-Takens point BT_3 has left our κ-region of interest, and instead a saddle-node Hopf point SH_3 has moved towards lower values of κ. Furthermore, a second saddle-node Hopf point SH_3 on H_3 also entered the κ-region of interest; in Fig. 6(f) these two points SH_3 lie very close to one another, and they are responsible for the changes from super- to subcritical of both S and H_3. As η is increased further, the two sets of saddle-node bifurcation curves, and the associated cusps points, converge to one another. Simultaneously, the loop of the subcritical part of H_3 decreases in size and converges to the cusp point on S; see Figs. 6(g) to (i). Note that the bifurcation diagram in the final panel (i) for $\eta = 0.9$ is a small perturbation of the degenerate double-covered case in Fig. 4(a) for $\eta = 1.0$. Details of the transition process towards $\eta = 1.0$ are presented in Sec. 4.3.

4.2 Transitions involving codimension-two points near $\eta = 0.0$

We now consider in more detail what happens to the two sets of codimension-two points SH_1 and SH_2 in Fig. 4(b) as η is increased. These two sets of points are identical for $\eta = 0.0$ (because of the additional π-periodicity of C_p), but they undergo two different transitions for $\eta > 0.0$. These are sketched in Figs. 7 and 8. The starting point is the interaction for $\eta = 0.0$ of the saddle-node curve S and Hopf curves H_1, H_2 and H_3 in codimension-two double-Hopf, saddle-node Hopf and Bogdanov-Takens bifurcation points as sketched in Fig. 7(a). When compared with Fig. 4(b), we note that the point BT_3 in Fig. 7(a) is outside the shown κ-range.

Figure 7 concerns bifurcations associated with the point SH_1 near $C_p = \pi$ in Fig. 4(b). The ensuing transition is quite simple: with increasing $\eta > 0$ the

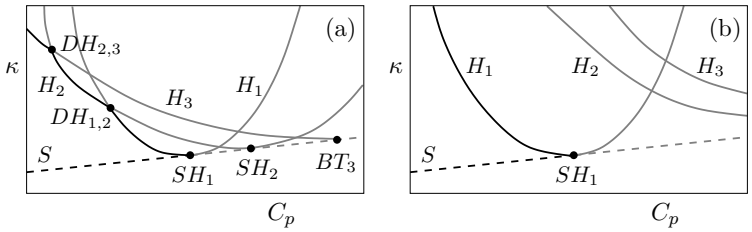

Figure 7: Sketch of the first type of interactions of double-Hopf DH, saddle-node Hopf SH and Bogdanov-Takens BT bifurcation points as η is increased from zero.

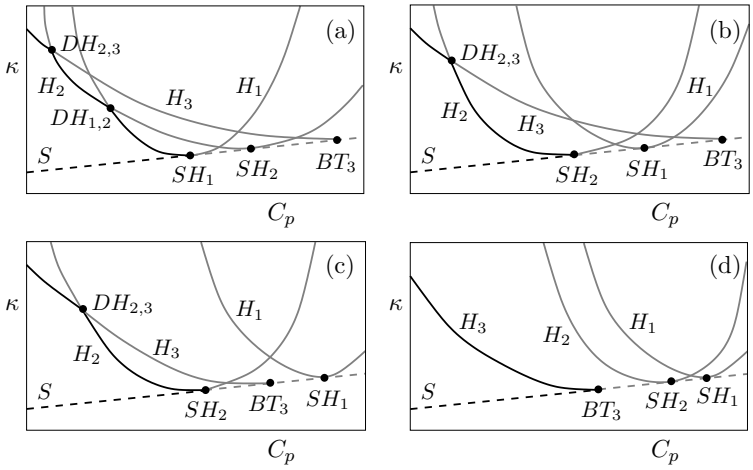

Figure 8: Sketch of the second type of interactions of double-Hopf DH, saddle-node Hopf SH and Bogdanov-Takens BT bifurcation points as η is increased from zero.

double-Hopf points $DH_{1,2}$ and $DH_{2,3}$ move rapidly up and out of our region of interest. At the same time, the points SH_2 and BT move up and to the right along the curve S. As a result, the Hopf curve H_1 is the only Hopf curve in the region of interest with a supercritical part, up to the point SH_1; see Fig. 7(b). The sketched situation is as that near SH_1 in the panels of Fig. 6.

The second transition, sketched in Fig. 8, concerns bifurcations associated with the point SH_1 near $C_p = 0$ in Fig. 4(b). Starting from the same situation in Fig. 8(a), as η is increased from zero the two saddle-node Hopf points SH_1 and SH_2 move closer together and the double-Hopf point $DH_{1,2}$ moves down along H_1. The three points then all come together in a degenerate saddle-node Hopf bifurcation point, after which SH_1 and SH_2 exchange positions along S and $DH_{1,2}$ disappears; see Fig. 8(b). Next the points SH_1 and BT_3 exchange their positions along S; see Fig. 8(c). This is the situation one finds for $\eta = 0.1$

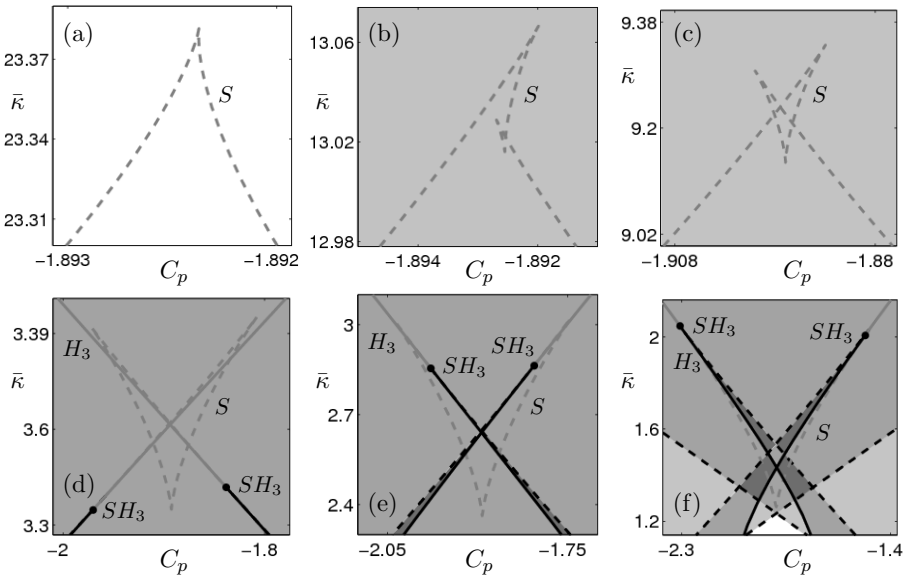

Figure 9: Emergence of cusp points on the saddle-node bifurcation curve S and their interaction with the Hopf curve H_3. From (a) to (f), η takes the values 0.51, 0.52, 0.53, 0.59, 0.63 and 0.75; the other parameters are as in Fig. 4.

in Fig. 6(a). When η is increased above $\eta = 0.1$, the points SH_2 and BT_3 also exchange their positions along S, which involves the disappearance of the double-Hopf point $DH_{2,3}$ as well. As a result, the curve H_3 is now the only curve with a supercritical part in the region of interest, and it ends at the Bogdanov-Takens point BT_3; see Fig. 8(d). This is exactly the situation we find in Fig. 6(b)–(e), where the point BT_3 has entered the relevant κ-range while SH_1 and SH_2 now lie outside this range.

The result of this, necessarily quite mathematical, discussion is a consistent picture near the special bifurcation diagram for $\eta = 0.0$, which involves several codimension-three bifurcations of ECMs in quick succession at η is increased.

4.3 Details of the transition to $\eta = 1.0$

We now investigate the emergence of the loop of the Hopf bifurcation curve H_3 in Fig. 6, its interaction with the saddle-node curve S and the subsequent convergence to the degenerate bifurcation diagram for $\eta = 1.0$. The associated changes to the bifurcation diagram are shown in Figs. 9 and 10. For $\eta \leq 0.4$ there are two distinct saddle-node curves. However, as the loop of H_3 develops, we find that these two curves connect (at infinity) and form a single curve S that has a cusp point at large values of κ; see Fig. 9(a). When η is increased further, one encounters a codimension-three swallow-tail singularity [12] that creates two further cusp points on the right-hand side of this (subcritical) saddle-node curve;

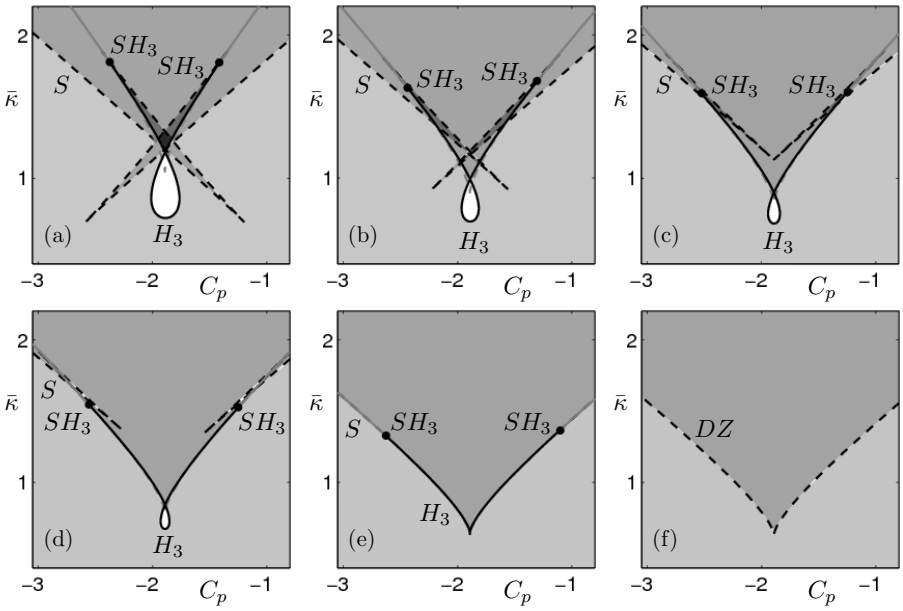

Figure 10: Details of the convergence of the supercritical loop of the Hopf curve H_3 to the degenerate case for $\eta = 1.0$. From (a) to (f), η takes the values 0.8, 0.85, 0.88, 0.9, 0.99 and 1.0; the other parameters are as in Fig. 4.

see Fig. 9(b). As η is increased further, one of the cusp points moves through the left branch of S, forming what looks like a down-pointing arrow, while this entire structure moves to lower values of κ; see Fig. 9(c). For $\eta \approx 0.59$ the structure starts to interact with the Hopf curve H_3, meaning that the saddle-node Hopf bifurcations SH_3 enter into the region near the cusp points; see Fig. 9(d). Increasing η further, the points SH_3 move up along S, as in Fig. 9(e), and then move (one by one) past the upper cusp points onto the parts of S between the cusp points; see Fig. 9(f). As a result, most of the curve S (with the exception of the 'arrow tip') is now supercritical and, hence, part of the ECM stability boundary; compare with Fig. 6(g). Notice also that the entire structure is inside the region of interest for $\eta \geq 0.6$.

Figure 10 illustrates in detail how the structure consisting of the cusp points on S and the supercritical loop of H_3 develops further as the degenerate case $\eta = 1.0$ is approached. Panel (a) is an enlargement of the situation for $\eta = 0.8$. As η is increased, the lower cusp points move towards larger values of κ and above the lowest cusp point on S; see Fig. 10(b). The two sets of two remaining cusp points (on the right and the left), and the associated short parts of S between them that contain the saddle-node Hopf points SH_3, move closer to the each other; see Fig. 10(c) and (d). With increasing η they disappear in swallowtail bifurcations, resulting in a situation as in Fig. 10(e) for $\eta = 0.99$. Notice also that the entire curve H_3 is now extremely close to S (the loop has

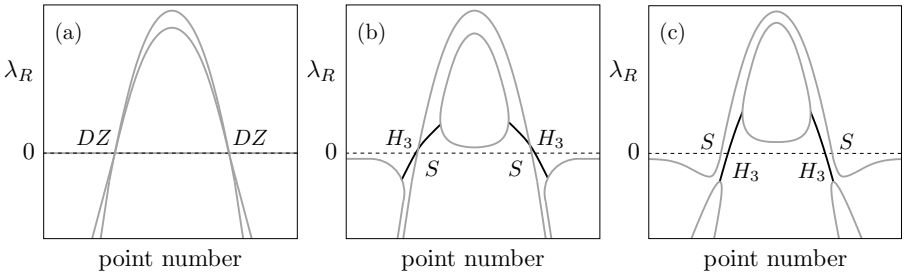

Figure 11: Continuation in C_p of the leading eigenvalues of an ECM, represented by their real parts as a function of the DDE-BIFTOOL point number; grey curves represent real eigenvalues and black curves complex-conjugate eigenvalues. Panel (a) is for $\eta = 1.0$, panel (b) is, for example, for $\eta = 0.99$ and $\kappa = 0.001$, and panel (b) is for $\eta = 0.99$ and $\kappa = 0.0015$; other parameters are as in Fig. 4.

shrunk down almost to the remaining cusp point on S). Indeed, the curves S and H for $\eta \approx 1.0$ are perturbations of the double eigenvalue zero curve DZ of the limit $\eta = 1.0$ in Fig. 10(f).

Figure 11 shows what this perturbation statement means on the level of the leading eigenvalues of the associated ECM as continued with DDE-BIFTOOL. In each panel we plot the real parts of the eigenvalues as a function of the DDE-BIFTOOL point number of the computed points in a continuation in the feedback phase C_p (for fixed κ). Along grey parts the respective eigenvalue is real, while black curves correspond to a pair of complex-conjugate eigenvalues. Figure 11(a) shows the continuation of the leading eigenvalues of the limiting and degenerate case of $\eta = 1.0$. There are two branches of real eigenvalues that cross the zero axis at the two double-zero points DZ. Notice further that there is a real eigenvalue zero independently of C_p (or the point number). We find that, in this (non-dimensionalized) representation, the eigenvalue spectrum for $\eta = 1.0$ does not depend on κ, as long as the curve DZ in Fig. 10(f) is indeed crossed (only twice). Figure 11(b) shows the perturbation of the leading eigenvalues for $\eta \approx 1.0$ for the case that the bifurcation diagram in Fig. 10(e) is crossed horizontally below SH_3, for example, for fixed $\kappa = 0.001$. The ECM is stable for large and small point numbers. It is destabilised (for increasing or decreasing point number or C_p) in the supercritical Hopf bifurcation H_3, which takes place just before the saddle-node bifurcation S. The associated pair of complex eigenvalues becomes real below and above H_3. Figure 11(c) shows the perturbation of the leading eigenvalues for $\eta \approx 1.0$ for the case that the bifurcation diagram in Fig. 10(e) is crossed above SH_3, for example, for fixed $\kappa = 0.0015$. The ECM is still stable for large and small point numbers, but this time it is destabilised (for increasing or decreasing point number or C_p) in the supercritical saddle-node bifurcation S, which takes place just before H_3. Again, the pair of complex eigenvalues becomes real below and above

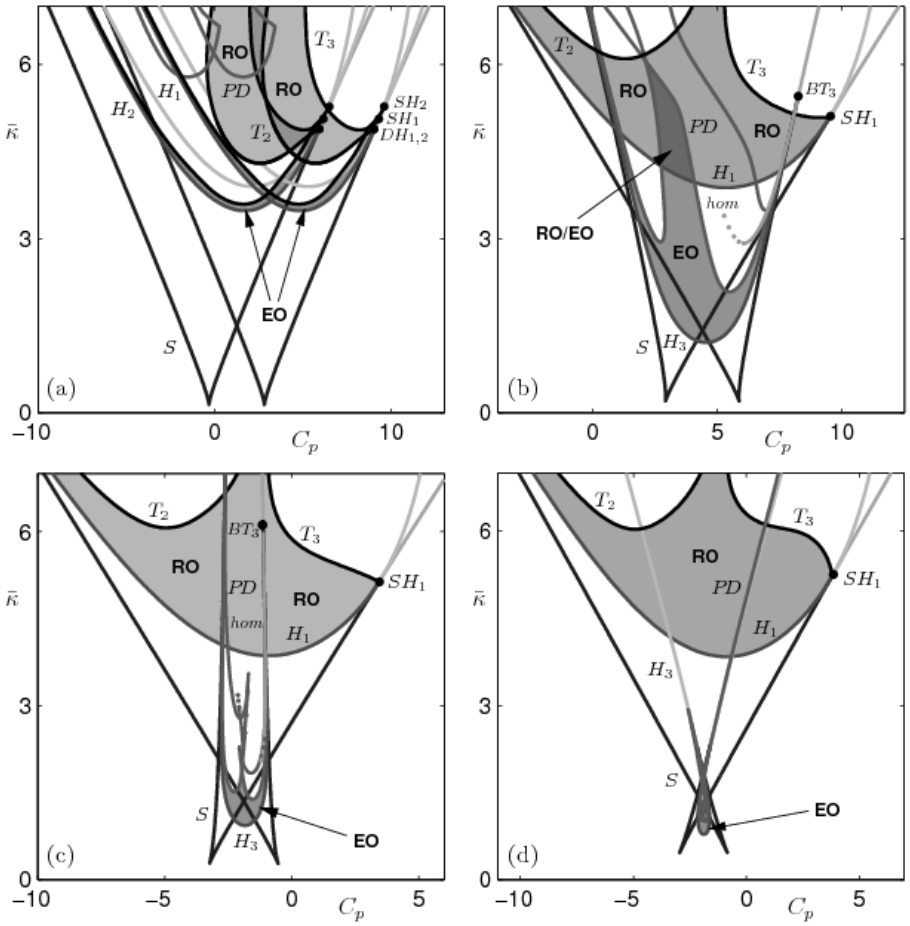

Figure 12: The two-parameter bifurcation diagrams of Eqs. (12)–(14) in the (C_p, κ)-plane with the stability regions of periodic solutions. Shown are curves of saddle-node bifurcation S, Hopf bifurcation H_i, period-doubling bifurcation PD, torus bifurcations (T_i), and homoclinic bifurcation hom; regions of stable ROs are shaded orange and regions of stable EOs are shaded blue, which different shading for overlap regions of coexisting stable per iodic solutions. From (a) to (d), η takes the values 0.0, 0.3, 0.5, and 0.7; the other parameters are as in Fig. 4.

H_3. Overall, Fig. 11 shows that in both cases the limit for $\eta = 1.0$ is reached as follows: the respective bifurcation points S and H_3 and the nearby points where two eigenvalues become complex converge to the point DZ. At the same time the three branches in Fig. 11(a) are approached by corresponding branches in Fig. 11(b) and (c).

5 Stability and bifurcations of periodic solutions

The changes of the ECM bifurcation diagram with the homotopy parameter η have immediate consequences for bifurcating periodic solutions. As was already mentioned, there are two different types of periodic intensity fluctuations. First, undamped relaxation oscillations that correspond to a periodic exchange of energy between the electric field and the inversion at a characteristic RO frequency of around 5 GHz;
ROs are present in all semiconductor lasers, and they can easily be undamped by external optical influences. Second, external round-trip oscillations, which are due to the travel of the light to the mirror and back to the laser. Hence, EOs generally have a much lower frequency — of around 500 MHz for the delay time $\tau = 500$ considered here. Both types of oscillations arise by crossing supercritical parts of Hopf bifurcation curves in the bifurcation diagrams of Figs. 4 and 6. The question arises which branches of Hopf bifurcations give rise to ROs and EOs, respectively, and how large their respective stability regions are. As Fig. 12 shows, the answer depends strongly on the homotopy parameter η. Shown are two-parameter bifurcation diagrams of the periodic solutions of Eqs. (12)–(14) in the (C_p, κ)-plane for four values of η. Specifically, we determined the stability regions of ROs and EOs by computing bifurcation curves of periodic solutions with the package `PDDE-CONT` [37], which is able to deal with the additional S^1-symmetry of the DDE. Apart from saddle-node and Hopf bifurcation curves, we also found curves of period-doubling bifurcations PD, of torus (or Neimark-Sacker) bifurcations T, and of homoclinic bifurcations hom. For ease of presentation we show one instance of the relevant part of the bifurcation diagrams in Fig. 12 over several periods of C_p.

For the special case of $\eta = 0$ in Fig. 12(a) there is a stability region of ROs that is bounded by two torus bifurcation curves T_2 and T_3, which emanate from the codimension-two points $DH_{1,2}$ and SH_1, respectively. We also find a very small region of EOs, which is bounded by the Hopf bifurcation curve H_2 and a torus bifurcation curve T_1. The latter curve emanates from the codimension-two saddle-node Hopf point SH_2 and closely follows H_2. Note that all bifurcation curves are shown twice in Fig. 12(a) due to the additional π symmetry for $\eta = 0$. As was shown in Fig. 7, when η is increased from zero, the double-Hopf point $DH_{1,2}$ moves rapidly up and to the left, leaving our region of interest. As it does so, it 'drags' the torus curve with it, so that the RO stability region rapidly grows in size and is now bounded by the Hopf bifurcation curve H_1 below and torus bifurcation curves T_2 and T_3 above. The shape and size of the RO stability region remains virtually unchanged when η is increased further; see Fig. 12(b)–(d). The situation is quite different for the EOs. The local change with η near the codimension-two points shown in Fig. 7, in combination with the curve H_3 moving towards lower values of κ, results for moderate amounts of cross feedback in an EO stability region of considerable size; see Fig. 12(b) for $\eta = 0.3$. This region is bounded below by the supercritical part of the Hopf bifurcation curve H_3 and above by a curve of period-doubling and a curve of homoclinic bifurcations (that emerges from BT_3). Notice that stable EOs

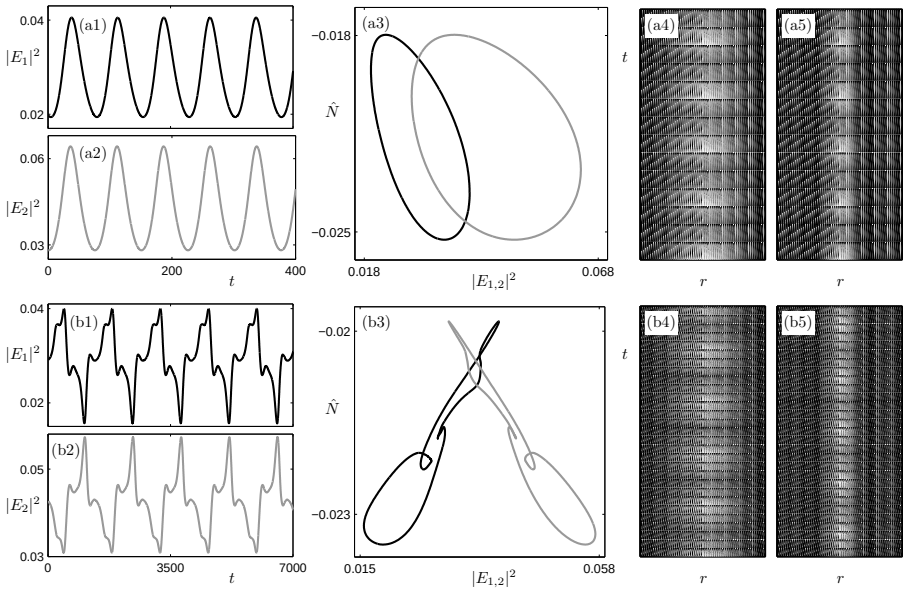

Figure 13: Coexisting relaxation oscillations in row (a), and external round-trip oscillations in row (b). Shown are time series (column 1) of the powers P_1 and P_2 of LP_{01} and LP_{02}, their projections into $(E_i, \hat{N})$-space (column 2), and the time series of the spatial intensity modes LP_{01} and LP_{02} of the laser (columns 3 and 4); $\eta = 0.3$, $C_p = \pi$ and $\kappa = 0.005$; the other parameters are as in Fig. 4.

occur for much lower values of κ compared to ROs. Furthermore, we find a large region of bistability between EOs and ROs for $\eta = 0.3$. As we have seen in Sec. 4.1, with increasing η the supercritical part of H_3 shrinks and moves to lower values of κ. It turns out that the curves of period-doubling and homoclinic bifurcations follow H_3, meaning that the EO stability region decreases dramatically as a result; see Fig. 12(c). As η approaches $\eta = 1.0$, this region effectively disappears near the lowest cusp point of the curve S; see Fig. 12(d).

Our results indicate that an experimental observation of EOs might be a practical way of testing for the existence of cross-coupling between the two transverse modes. Once EOs are found, a more ambitious goal would be to actually map out experimentally the size of the EO stability region as a function of both κ and C_p. It should be quite straightforward to distinguish EOs from ROs, as EOs have a much lower frequency (which also makes it easier to measure them [1]). However, there is another distinguishing feature, which is illustrated in Fig. 13 with specific examples of simultaneously stable ROs and EOs from the bistable region for $\eta = 0.3$ in Fig. 12(b). ROs are characterized by fast oscillations, where the two electric fields with amplitudes P_1 and P_2 are in phase; see Fig. 13(a1) and (a2). By contrast, EOs are slower oscillations (notice

the difference in scale of the t-axes), where the two electric fields with amplitudes P_1 and P_2 are in anti-phase; see Fig. 13(b1) and (b2). A physical interpretation of the anti-phase behaviour of the EOs might lie in the fact that the modes LP_{01} and LP_{02} compete for the spatial carrier source on a time scale that agrees with the diffusion time: one mode exhausts the carriers and then decays; while the carriers diffuse back, the other mode has a slightly larger overlap with the replenishing carrier profile, so that it starts lasing first, and the process repeats. We remark that on the level of the total spatial intensity of the laser, the individual maxima and minima of P_1 and P_2 add up for ROs, but they cancel each other out for EOs, leading to a less pronounced oscillation of the total laser power.

Figure 12 shows that ROs and EOs destabilize when the feedback strength κ in increased. Two examples in [15] illustrate that this may lead to more complicated dynamics of the two modes involved: motion on an invariant torus bifurcating from ROs, and chaotic spatial mode dynamics after a period-doubling sequence starting from stable EOs. In both cases the respective in-phase or anti-phase dynamic was shown to be preserved.

6 Discussion

When one wants to model and study the dynamics of transverse spatial optical modes, that is, patterns of light, in a laser subject to optical feedback then two ingredients are crucial. Firstly, one needs a mathematical description of the interaction of the spatial modes via their common spatial carrier reservoir that is provided by electric pumping and carrier diffusion. We considered here the case of a vertical-cavity surface-emitting laser with cylindrical geometry and a disk-shaped aperture. Starting from a spatial rate equation model due to [41], we used a mode expansion in linearly polarized LP modes of a cylindrical waveguide. After discretization of the spatial carrier reservoir by Fourier modes, one obtains a system of ODEs that describes the dynamics of the LP modes (up to a given order and for both polarizations) inside the disk-shaped active region. Secondly, the feedback enters into the equation of the electric field of each mode, and it should be a function of the delayed electric fields of all modes. It is a major open question how each mode is influenced by itself and by the other modes as a result of the optical feedback from an external mirror. Note that in all previous studies pure self-feedback of the modes had been assumed. However, at least some cross-feedback between the modes via the feedback loop is likely to occur. Therefore, we model cross-feedback between modes by the introduction of additional homotopy parameters. This setting is still very general: the overall model is a (possibly quite large) DDE with (possibly very many) homotopy parameters in the feedback terms.

However, if one considers a VCSEL with only a few modes then the resulting DDE model may be small enough to allow for a bifurcation analysis with advanced numerical tools. In particular, the effect of self- versus cross-feedback of the different modes (as modeled by the homotopy parameters) can then be

investigated. We studied here as a concrete example a VCSEL with COF that supports only the first two rotationally symmetric LP modes; the expanded system of ODE has dimension 18, and a single homotopy parameter η suffices to describe the amount of self- versus cross-feedback. The resulting DDE system is just small enough for numerical continuation tools and, in particular, it allows for the computation of the eigenvalue spectrum of periodic solutions. This allowed us to investigate how the stability regions of the external-cavity modes and bifurcating periodic solutions, in the plane of feedback phase C_p and feedback strength κ, depend on the homotopy parameter η — all the way from pure self-feedback to pure cross feedback. We found a consistent bifurcation scenario that involves bifurcations of higher codimension, which, in effect, constitutes a three-parameter study of the stability properties of the two-mode VCSEL.

Our bifurcation analysis revealed specific results that are of interest from the physical point of view. First of all, we found large regions of coexistence between stable ECMs, and this multistability might be useful for application, for example, in all-optical flip-flop schemes. Moreover, we identified the existence of two distinct types of periodic solutions. The characteristic relaxation oscillations can be found for sufficiently large feedback strength κ for any value of η. However, we also found external round-trip oscillations, which show antiphase dynamics of the two spatial modes on the timescale of the delay time. Importantly, EOs occur stably (in physically accessible regions of the (C_p, κ)-plane) only for low to intermediate values of η, that is, for moderate amounts of cross-feedback. Therefore, the bifurcation analysis suggests that in a two-mode VCSEL an experimental observation of EOs may be used as an indication of the amount of cross-coupling via the feedback loop.

An obvious challenge would be the study of VCSELs with general (not rotationally symmetric) spatial modes. In this case the polarization of the modes will also play a role. The resulting DDE models will necessarily be quite a lot more involved, but the bifurcation analysis of ECMs in the presence of feedback may already be feasible for small numbers of spatial modes. Furthermore, the experimental verification of model predictions of VCSEL dynamics remains a considerable challenge. However, recent experiments in [2] have shown that individual spatial modes of a VCSEL can be stabilized via polarization- and frequency-selective feedback. Furthermore, high-speed imaging techniques as described in [1] might be a way of measuring osciallatory mode dynamics.

Acknowledgments

The work of K.G. was supported under the *Dynamics of Patterns Programme* of the Netherlands Organization for Scientific Research (NWO) and the Foundation for Fundamental Research on Matter (FOM).

References

[1] Barchanski A., Genstry T., Degen C., Fischer I. and Elsäßer W. [2003] "Picosecond Emission Dynamics of Vertical-Cavity Surface-Emitting Lasers: Spatial, Spectral, and Polarization-Resolved Characterization," *IEEE Quantum Elec.* **39** 850–858.

[2] Chembo, Y. K., Mandre S. M., Fischer I., Elsäßer W. and Colet P. [2009] "Controlling the emission properties of multimode vertical-cavity surface-emitting lasers via polarization- and frequency-selective feedback" *Phys Rev A* **79**, 013817.

[3] Chong C. H. & Sarma J. [2003] "Lasing Mode Selection in Vertical-Cavity Surface-Emitting Lasers," *IEEE Photon. Tech. Lett.* **5**, 761–764.

[4] Degen C., Krauskopf B., Jennemann G., Fischer I. and Elsäßer W. [2000] "Polarization selective symmetry breaking in the near-fields of vertical cavity surface emitting lasers," *J. Opt. B: Quantum Semiclass. Opt.* **2**, 517–525.

[5] Dellunde J., Valle A. & Shore K. A. [1996] "Transverse-mode selection in external-cavity vertical-cavity surface-emitting laser diodes," *J. Opt. Soc. Am. B* **13**, 2477–2483.

[6] Doedel E., Champneys A., Farigrieve T., Kuznetsov Y., Sandstede B. and Wang X. [1997] "AUTO 97: Continuation and Bifurcation Software for Ordinary Differential Equations" `http://indy.cs.concordia.ca/auto/main.html`.

[7] Engelborghs K., Luzyanina T., Samaey G. and Roose D. [2001] "DDE-BIFTOOL: a Matlab package for bifurcation analysis of delay differential equations," Tech. Rep. TW-330 Department of Computer Science, K. U. Leuven, Belguim `http://www.cs.kuleuven.ac.be/cwis/research/twr/research/software/delay/ddebiftool.shtml`.

[8] Erneux T., Rogister F., Gavrielides A. and Kovanis V. [2000] "Bifurcation to mixed external cavity mode solutions for semiconductor lasers subject to optical feedback," *Opt. Commun.* **183**, 467–477.

[9] Erzgräber H., Krauskopf B. and Lenstra D. [2006] "Compound laser modes of mutually delay-coupled lasers," *SIAM J. Appl. Dyn. Syst.* **5**, 30–65.

[10] Guckenheimer J. and Holmes P. [1983] *Nonlinear Oscillations, Dynamical Systems, and Bifurcations of Vector Fields*, (Springer-Verlag, New York).

[11] Fischer I., Heil T. and Elsäßer W. [2005] "Emission dynamics of semiconductor lasers subject to delayed optical feedback: an experimentalists perspective," in [24], pp. 218–237.

[12] Fowler D. H. and Thom R. [1989] Structural stability and morphogenesis: an outline of a general theory of models (Westview Press, Boulder Colorado).

[13] Green K. [2009] "Stability near threshold in a semiconductor laser subject to optical feedback: A bifurcation analysis of the Lang-Kobayashi equations," *Physical Review E* **79**, 036210.

[14] Green K., Krauskopf B. and Lenstra D. [2007] "External cavity mode structure of a two-mode VCSEL subject to optical feedback," *Opt. Commun.* **277**, 359–371.

[15] Green K., Krauskopf B., Marten F. and Lenstra D. [2008] "Bifurcation analysis of a spatially extended laser with optical feedback," *SIAM J. Appl. Dynam. Syst.* **8**, 222–252.

[16] Haegeman B., Engelborghs K., Roose D., Pieroux D. & Erneux T. [2002] "Stability and rupture of bifurcation bridges in semiconductor lasers subject to optical feedback," *Phys. Rev. E* **66**, 046216.

[17] Hale J. K. & Verduyn Lunel S. M. [1993] *Introduction to Functional Differential Equations* (Springer-Verlag, New York).

[18] Heil T., Fischer I., Elsäßer W., Krauskopf B., Green K. and Gavrielides A. [2001] "Delay dynamics of semiconductor lasers with short external cavities: Bifurcation scenarios and mechanisms," *Phys. Rev. E* **67**, 066214.

[19] Heil T., Fischer I., Elsäßer W., Krauskopf B., Green K. and Gavrielides A. [2003] "Delay dynamics of semiconductor lasers with short external cavities: bifurcation scenarios and mechanisms", *Phys. Rev. E* **67**, 066214).

[20] Hess O. [2000] "Thery and Simulation of spatially extended semiconductor lasers," in [24], pp. 173-190. pp. 128–148.

[21] Homar M., Moloney J. V. and San Miguel M. [1996] "Travelling wave model of a multimode Fabry-Perot laser in free running and external cavity configurations," *IEEE J. Quantum Electron.* **32**(3), 553–566.

[22] Kane D. M. and Shore K. A. [2005] *Unlocking Dynamical Diversity: Optical Feedback Effects on Semiconductor Lasers* (Wiley).

[23] Krauskopf B. [2005] "Bifurcation analysis of lasers with delay," in [22], pp. 147-183.

[24] Krauskopf B. and Lenstra D. [2000] *Fundamental Issues of Nonlinear Laser Dynamics*, AIP Conf. Proc. Vol. 548 (American Institute of Physics Publishing, Melville, NY).

[25] Krauskopf B., Van Tartwijk G. H. M. and Gray G. R. [2000] "Symmetry properties of lasers subject to optical feedback," *Opt. Commun.* **177**, 347.

[26] Kuznetsov Yu. [2004] *Elements of Applied Bifurcation Theory* Third Edition (Springer-Verlag, New York).

[27] Kyrychko Y. N., Hogan S. J., Gonzalez-Buelga A. and Wagg D. J. [2007] "Modelling real-time dynamic substructuring suing partial delay differential equations," *Proc. R. Soc. A* **463**, 1509–1523.

[28] Lang R. and Kobayashi K. [1980] "External optical feedback effects on semiconductor injection laser properties," *IEEE J. Quantum Electron.* **16**(3), 347–355.

[29] Lenstra D., Verbeek B. H. and den Boef A. J. [1985] "Coherence collapse in single-mode semiconductor lasers due to optical feedback," *IEEE J. Quantum Electron.* **21**, 674–679.

[30] Mork J., Mark J. and Tromborg B. [1990] "Route to chaos and competition between relaxation oscillations for a semiconductor laser with optical feedback," *Phys. Rev. Lett.* **65**, 1999–2002.

[31] McInerney J.G., O'Brian P, Skovgaard P., Mullane M., Houlihan J., O'Neil E., Moloney J.V. and Indik R.A. [2000] "High brightness semiconductor lasers with reduced filamentation," in [24], pp. 173–190.

[32] Olesen H., Osmundsen J. H. and Tromborg B. [1986] "Nonlinear Dynamics and Spectral Behavior for an External Cavity Laser," *IEEE J. Quantum Electron.* **22**(6), 762–773.

[33] Onishi Y., Nishiyama N., Caneau C., Koyama F. and Zah C.-E. [2006] "All-Optical Regeneration Using Transverse Mode Switching in Long-Wavelength Vertical-Cavity Surface-Emitting Lasers," *Jap. J. Appl. Phys.* **45**, 467–468.

[34] Postlethwaite C. M. and Silber M. [2007] "Spatial and temporal feedback control of traveling wave solutions of the two-dimensional complex Ginzburg-Landau equation," *Physica D* **236**, 65–74.

[35] Roose D. and Szalai R. [2007] "Continuation and bifurcation analysis of delay differential eqautions," in Krauskopf B., Osinga H. M. and Galán-Vioque J. (Eds.) *Numerical Continuation Methods for Dynamical Systems: Path following and boundary value problems*, (Springer-Verlag, New York), pp. 359–399.

[36] Rottschäfer V. and Krauskopf B. [2007] "The ECM-backbone of the Lang-Kobayashi equations: A geometric picture," *Int. J. Bif. and Chaos* **17**(5), 1575–1588.

[37] Szalai R. [2005] "PDDE-CONT: A continuation and bifurcation software for delay-differential equations," Budapest University of Technology and Economics, Hungary `http://www.mm.bme.hu/~szalai/pdde`

[38] Tanguy Y., Ackemann T. and Jäger R. [2006] "Characteristics of bistable localized emission states in broad-area vertical-cavity surface-emitting lasers with frequency-selective feedback," *Phys. Rev. A* **74**, 053824.

[39] Topaz C.M., Porter J. and Silber M. [2004] "Multifrequency control of Faraday wave patterns," *Phys. Rev. E* **70**, 066206.

[40] Torre M. S., Masoller C., and Mandel P. [2002] "Transverse-mode dynamics in vertical-cavity surface-emitting lasers with optical feedback," *Phys. Rev. A* **66**:053817.

[41] Valle A. [1998] "Selection and modulation of high-order transverse modes in vertical-cavity surface-emitting lasers," *IEEE J. Quantum Electron.* **34**, 1924–1932.

[42] Wieczorek S., Krauskopf B., Simpson T. B. and Lenstra D. [2005] "The dynamical complexity of optically injected semiconductor lasers," *Phys. Reports* **416**, 1–128.

[43] Yu S. F. [2003] *Analysis and Design of Vertical Cavity Surface Emitting Lasers* (Wiley).